Journal of The Electrochemical Society, **163** (7) H491-H498 (2016)
0013-4651/2016/163(7)/H491/8/$33.00 © The Electrochemical Society

Structure-Dependent Electrochemistry of Reduced Graphene Oxide Monolayers

Christian Punckt,[a,b,c] Michael A. Pope,[a,b,d] Yifei M. Liu,[a,e] and Ilhan A. Aksay[a,z]

[a]*Department of Chemical and Biological Engineering, Princeton University, Princeton, New Jersey 08544, USA*
[b]*Vorbeck Princeton Research Center, Vorbeck Materials Corp., Monmouth Junction, New Jersey 08852, USA*

While graphene and other carbonaceous nanomaterials have shown promise in a variety of electrochemical applications, measurement of their intrinsic performance is often confounded with effects related to the complexities due to diffusion in a porous medium. To by-pass this limitation, we use effectively non-porous tiled monolayers of reduced graphene oxide as a model platform to study how rates of heterogeneous electron transfer evolve as a function of graphene structure/chemistry. A variety of electrochemical systems are investigated including the standard ferri/ferrocyanide redox probe, several common biomolecular redox systems as well as copper electrodeposition. We show that the rates of heterogeneous electron transfer can vary by as much as 3 orders of magnitude depending on the reduction or annealing conditions used and the redox system investigated. Performance changes are linked to graphene chemistry, and we show that the graphene oxide reduction procedure must be chosen judiciously to maximize the electrochemical performance for particular applications.

Manuscript submitted January 18, 2016; revised manuscript received March 24, 2016. Published April 6, 2016.

As with all carbonaceous materials in the past (nanodiamond, fullerenes, carbon nanotubes), the latest addition to the carbon materials family, "graphene", has generated a tremendous amount of activity in the scientific community and in particular among electrochemists.[1–7] Besides their remarkable electronic, thermal, and mechanical properties, the electrochemical performance of various types of graphene has been touted as superior to more classical electrode materials such as metals, graphite, or glassy carbon. However, the intrinsic electrochemical properties of graphene have been difficult to access, as the effects of roughness and porosity of drop-cast electrode films often dominate the observed behavior.[8–10] This makes a meaningful comparison both with classical, flat electrodes such as glassy carbon (that do not show porosity- or roughness-related artefacts that can be interpreted as catalytic effects), but also with other carbon nanomaterials (with similar but different degree of roughness and porosity) difficult to impossible, unless special precautions or measurement techniques are applied.[11–13] Instead of effects that are directly related to differences in the kinetics of heterogeneous electron transfer (HET), differences in electrode morphology are being measured and compared, often unknowingly.

In order to establish a basis for comparison of different graphene-based materials, we have recently devised and validated an experimental procedure for electrochemical measurements with graphene-based electrodes that relies on films of densely tiled individual graphene sheets coated onto substrates with inherently slow electron transfer kinetics.[14] Using this approach, we were able to reduce morphology-related artefacts sufficiently, such that the intrinsic electrochemical properties related to electron transfer kinetics became evident using standard voltammetric techniques.[11,15] In our prior work, we demonstrated the reliability of this approach and that roughness and porosity indeed may dominate electrochemical measurements as one moves from a well-defined, tiled monolayer to, e.g., porous drop-cast films.[10,11]

In this work, we use our method to systematically study different types of graphene-based materials in comparison to glassy carbon and highly-oriented pyrolytic graphite (HOPG). The chemistry of the graphene-based material was tuned, both through thermal and electrochemical reduction of graphene oxide. Using different degrees of thermal reduction, we can tune the oxygen content and lattice disorder of the material within certain boundaries (Fig. 1), yielding reduced graphene-based materials with oxygen contents between over 35 (for as-prepared graphite oxide (GO)[16]) and less than 1 mol%. Oxygen-containing functional groups and the lattice vacancies generated during thermal treatment, as carbon is removed from the lattice in the form of CO and CO_2, lead to a high density of defects in the otherwise pristine graphene lattice. These disruptions to the graphene lattice are indicated by a high I_D/I_G ratio[15,17–19] measured by Raman spectroscopy. With increasing reduction and annealing temperature beyond ~1300°C, the number density of functional groups and lattice defects progressively decreases. At the highest reduction and annealing temperatures, the material structure approaches that of pristine graphene with relatively large domains of sp^2-bonded carbon atoms in hexagonal configuration, as indicated by low I_D/I_G ratio[15] (Fig. 1a) and the disappearance of characteristic lines in the Fourier-transform infrared spectroscopy (FTIR) spectra (Figs. 1b–1c) associated with the presence of different types of functional groups.[18,20–25]

We refer to our material as "functionalized graphene sheets" (FGSs) due to the remaining oxygen-containing functional groups at the edge, at lattice (vacancy) defects, and on the plane of the material (Fig. 1b).[18,26,27] The degree of reduction can be indicated by a suffix x (FGS_x), representing the molar ratio of carbon to oxygen (C/O ratio) in the material, with graphene oxide and pristine graphene corresponding to FGS_2 and FGS_∞, respectively. However, x is not a unique indicator of material properties since the types of functional groups, lattice defects and their spatial distribution depend on the specific oxidation and reduction path used and undoubtedly impact their electrochemical properties. In Table I, we show an overview of the types of FGSs used in this work.

Our electrochemical testing using ferro/ferricyanide and common biomolecular redox probes reveals that, depending on the type of graphene, rates of HET vary in a wide range. In particular with respect to biomolecules, highly functionalized graphene is found to specifically interact with the redox probes, leading to adsorption behavior. Our study highlights, that while graphene-based materials derived from graphene oxide can be tuned to achieve the best results with respect to particular redox probes, the resulting rate of electron transfer rarely exceeds that of glassy carbon. Graphene-based electrodes can be used to their full potential, however, by combining materials with maximal intrinsic properties (as determined herein) with custom-designed morphology to achieve optimum performance in various applications including sensing, electrocatalysis, metal plating, etc.

Methods

Processing of FGSs.—GO was prepared according to the method of Marcano et al.[28] (Tour's method). Three cycles of centrifugation and washing in de-ionized (DI) water were used to separate GO from the

[c]Present Address: Institute of Nanotechnology, Karlsruhe Institute of Technology, 76131 Karlsruhe, Germany.
[d]Present Address: Department of Chemical Engineering, University of Waterloo, Waterloo, Ontario, Canada N2L 3G1.
[e]Present Address: Department of Chemical and Biomolecular Engineering, University of California, Berkeley, California 94720, USA.
[z]E-mail: iaksay@princeton.edu

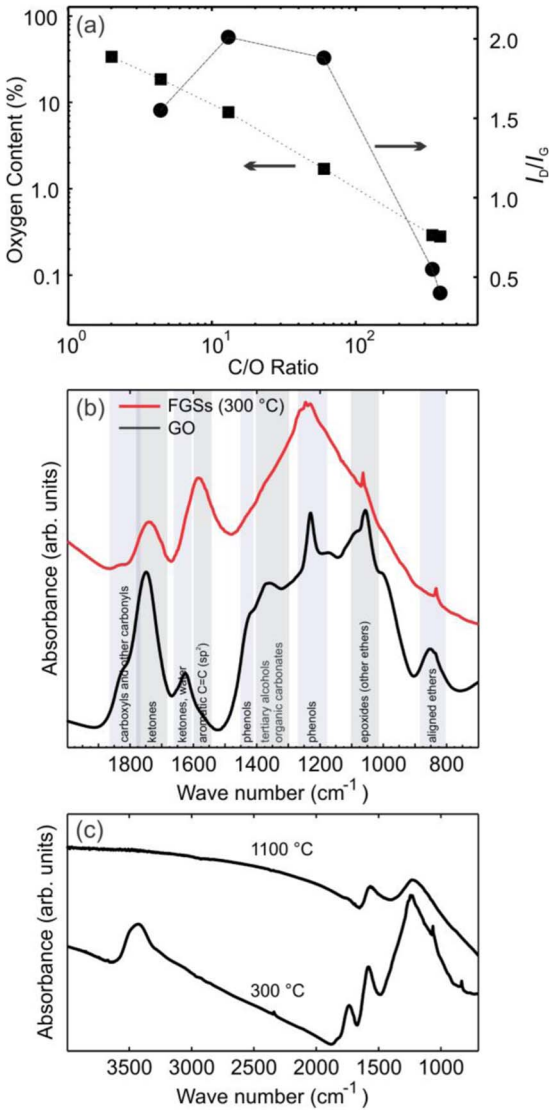

Figure 1. Characterization of thermally reduced graphene oxide powders. (a) Oxygen content in percent and ratio of the Raman I_D and I_G peaks as a function of C/O ratio for thermally reduced FGSs, data from reference.[15] (b) FTIR spectra of graphite oxide and mildly thermally reduced GO. The so-called fingerprint region is shown, and lines are associated with the corresponding structural features of FGSs according to the partly controversial literature.[20–25] (c) Comparison of complete FTIR spectra of mildly (FGS_4, 300°C) and more strongly (FGS_{13}, 1100°C) thermally reduced FGSs, indicating the loss of oxygen-containing functional groups.

soluble components of the reaction mixture. GO powder was obtained by spray-drying of the purified suspension. For thermal exfoliation of GO, about 200 mg of spray-dried GO were placed at the bottom of a fused silica tube and dried overnight in a flow of nitrogen. The tube was then evacuated and purged with argon (Grade 5.5, Air Products) three times. It was then evacuated once more and rapidly inserted into a tube furnace (Lindberg/Blue M, SPX Thermal Product Solutions) at temperatures between 300°C (resulting in C/O = 4) and 1100°C (C/O = 13) where it remained for 60 s (and 300 s for C/O = 60). Annealing consisted of heating thermally exfoliated powder for 1 h inside of a graphite furnace (Astro-1000, Thermal Technologies) at 1100°C (C/O = 340) and 1500°C (C/O = 385) under argon. Electrochemical reduction of FGS_2 monolayers was conducted in a 1 M aqueous solution of potassium chloride by cycling the monolayer electrode between open circuit potential (OCP) and negative potentials between −0.8 and −1.25 V vs. Ag/AgCl. This material will be referred to as erFGS.

FGS characterization.—Exfoliated and reduced GO powder was characterized using energy-dispersive X-ray spectroscopy (EDS, INCA x-act, Oxford Instruments, attached to a Vega 1 scanning electron microscope (SEM, Tescan USA)) to determine the oxygen content (confirmed by combustion-based analysis), by FTIR (Nexus 670, Thermo Nicolet, Madison, WI, equipped with a liquid nitrogen-cooled MCT/A detector) to elucidate the nature of oxygen-containing functional groups, and by Raman spectroscopy (Kaiser Optics, $\lambda = 532$ nm) to assess the defectiveness of the carbon lattice. The Raman spectra were fit using the Breit-Wigner-Fano (BFW) line shape for the G-peak and a Lorentzian fit for the D-peak.

Samples for EDS and Raman spectroscopy were prepared by mechanical pressing of pellets, each containing about 10 mg of material, using a 7 mm diameter die. FTIR samples were made by first mixing (reduced) GO powder with dry, high-purity potassium chloride powder (XL Ultra Pure Spectrograde KBr, International Crystal Laboratories, ICL) inside an argon-filled glove box using agate mortar and pestle. The resulting, roughly mixed powder was filled into a stainless steel capsule together with an agate ball and inserted into a grinding mill ("Wig-L-Bug", ICL) for 60 s. Still inside the glove box, the powder was then pressed into 7 mm diameter optical-quality pellets using a hydraulic press with a stainless steel die set (ICL). The pellets were sealed in a polymer bag and – while still under argon – transferred to the FTIR spectrometer, where they were unpacked and quickly inserted into the nitrogen-filled measurement chamber. Sample preparation and characterization under inert atmosphere was found to be critical in particular for highly hydrophilic non-reduced GO samples. FTIR measurements were performed in transmission.

Electrode preparation.—Monolayers were prepared using a Langmuir-Blodgett trough (Nima Technology) and deposited onto freshly cleaved HOPG substrates (Grade 2, Structure Probe) and flame-annealed gold films on silicon wafers according to prior work.[14] Briefly, reduced GO powder was first ultrasonically dispersed in 1,2-dichloroethane to separate the material into mostly single FGSs and to facilitate spreading of the sheets at the air-water interface. The floating sheets were compressed with the moveable barriers of the Langmuir-Blodgett trough such that the films were densely tiled but not significantly overlapping which resulted in a surface coverage of ∼90%.[15] Films of (non-reduced) graphene oxide were deposited from a 1:5 water to methanol dispersion in a similar way. Coated samples were air-dried for 10 min and then placed on a hot plate at 80°C until use. Prior to use, gold substrates coated with FGSs were transferred into a 1 mM solution of hexadecanethiol in ethanol in order for

Table I. Overview of graphene materials used in this study.

Material	Method of reduction	C/O	Oxygen content (mol%)	I_D/I_G
FGS_2	none	<1.8	>35	-
FGS_4	thermal exfoliation, 300°C, 60 s	4.4	18.5	1.55
FGS_{13}	thermal exfoliation, 1100°C, 60 s	13	7.7	2.01
FGS_{60}	thermal exfoliation, 1100°C, 300 s	60	1.7	1.88
FGS_{340}	as FGS_{13} plus annealing @ 1100°C, 1 h	340	0.29	0.55
FGS_{385}	as FGS_{13} plus annealing @ 1500°C, 1 h	385	0.28	0.40
erFGS	electrochemical	≈10	4.0	-

exposed gold surface to become passivated.[14] Immediately before use, such samples were rinsed with isopropanol and DI water and blow dried under a stream of high purity nitrogen. As-prepared monolayer electrodes were periodically examined by atomic force microscopy (AFM), SEM and optical microscopy for quality control purposes. As discussed in our previous works[14,15,26], FGSs obtained by thermal annealing exhibit diameters between a few 100 nm and about 2 μm, as well as a minimum thicknesses of 1–2 nm with some wrinkles and folds that introduce roughness on the order of 5–25 nm depending on the annealing conditions.[15] This means that the monolayer films are comprised of a mixture of densely tiled single and few-layer graphene. Though not atomically flat, results of electrochemical experiments conducted with such electrodes closely approach those obtained with a perfectly planar electrode.[9] Tiled monolayers obtained from graphene oxide exhibit considerably less roughness and are composed of mostly monolayer sheets with diameters of 1 to 5 μm.[14]

Electrochemical setup and procedures.—All electrochemical measurements as well as the electrochemical reduction of FGS_2 were conducted in custom-made Teflon cells,[14] accommodating the monolayer electrode as well as a Pt mesh counter electrode and a Ag/AgCl reference electrode and were controlled using a Biologic SP-300 potentiostat. The geometric area of the working electrode was defined by a perfluoroelastomer O-ring (Kalrez, McMaster-Carr) used to seal the cell. The area was 0.22 cm^2 as determined by measuring the imprint of the O-ring using optical microscopy and SEM. Electrolytes were prepared immediately prior to use, using DI water (Millipore) and as-received chemicals. All redox probes were present in the electrolytes at concentrations of 2.5 mM. For the ferro/ferricyanide redox couple, the supporting electrolyte was 1 M KCl. For nicotinamide adenine dinucleotide (hydrogen) (NADH), ascorbic acid (AA), dopamine (DA) and uric acid (UA) solutions, phosphate buffered saline at pH 7 was employed as supporting electrolyte whose total salt concentration was adjusted to 1 M through the addition of KCl in order to minimize Ohmic drops.

Cyclic voltammetry measurements with the ferro/ferricyanide redox probe were performed according to the following protocol: Initially, the electrode was allowed to rest at open circuit voltage for 5 s, and an Ohmic drop compensation measurement was performed by recording cell impedance at 50 kHz. Subsequently, the working electrode was set to a potential of 0 V vs. Ag/AgCl for 30 s. Then, starting at 0 V vs. Ag/AgCl, CVs were recorded within a potential window between −0.2 and +0.6 V vs. Ag/AgCl at scan rates between 50 and 2000 mV/s, each interrupted by resting periods at 0 V vs. Ag/AgCl of 60 s. This strict protocol was found to be beneficial for achieving good correspondence with cyclic voltammetry simulations (see below). For measurements with other redox probes, such as AA, appropriate start potentials and potential windows were individually adjusted, and a scan rate of 100 mV/s was used. In experiments with the ferro/ferricyanide redox probe, electrochemical impedance spectroscopy (EIS) data were collected at the equilibrium potential (zero current, typically near 240 mV vs. Ag/AgCl) and frequencies between 200 kHz and 1 Hz immediately following cyclic voltammetry measurements.

Electrodeposition of copper was performed in a solution of 200 g/L of hydrated copper sulfate with an added 50 g/L of sulfuric acid. The pH was adjusted sufficiently low to avoid any oxide formation.[29,30] Also, 20 g/L of HCl was added to stabilize Cu^+ ions near the surface through chloride complex formation and thus to facilitate deposition. A mercury sulfate electrode was used as reference and a high purity copper wire as counter electrode. A two-step deposition protocol was followed: First a potential of −0.65 V was applied for 100 ms to cause the formation of metallic copper nuclei. This was followed by deposition at a fixed current of −5 μA (resulting in varying potentials on the order of a few tens of mV) to grow the nucleated copper particles to detectable size while avoiding further nucleation events. After deposition, samples were immediately rinsed with DI water, dried under a flow of nitrogen, and transferred to the SEM for imaging.

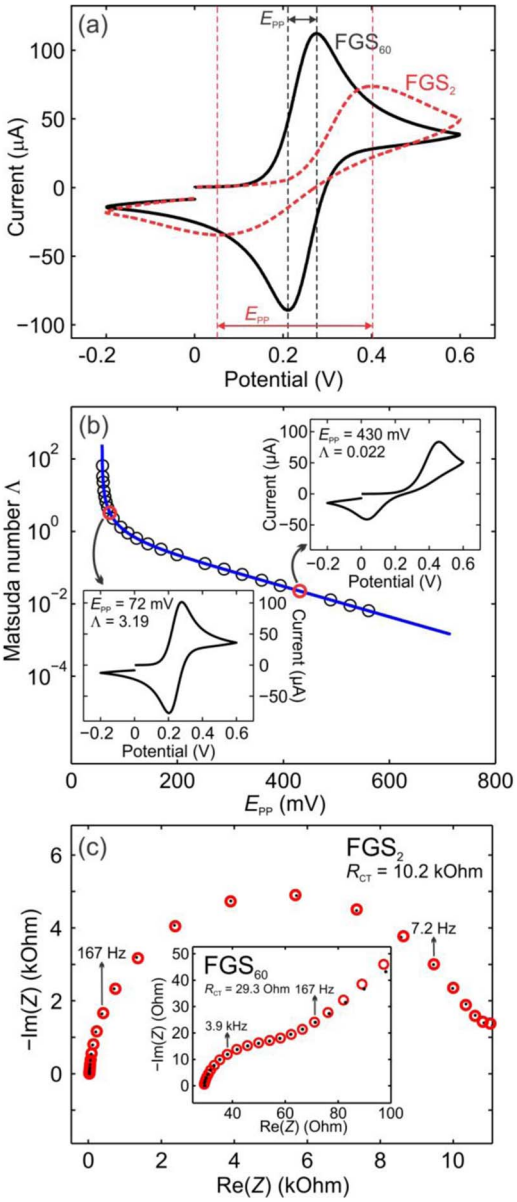

Figure 2. Electrochemical measurement protocols and data analysis using ferro/ferricyanide as redox probe obtained with FGS monolayer on passivated gold. (a) Representative examples of CVs obtained with the ferro/ferricyanide redox probe at a scan rate of 100 mV/s for two types of FGSs. The vertical dashed lines indicate the positions of the oxidation and reduction peaks, showing the meaning of E_{PP}. (b) Relation between E_{PP} and Λ determined computationally. The insets show individual simulated CVs for particular simulation conditions. Black circles indicate data points of the simulation. The blue line has been generated through spline interpolation of the data. (c) EIS data corresponding to the CVs shown in (a). Black dots: PEIS data from measurements with FGS_2 and FGS_{60} (inset). Red circles: Result of data fitting for the determination of R_{CT}.

Calculation of rate constants.—Cyclic voltammetry and EIS were used to determine the rate of HET k_0 with respect to the ferro/ferricyanide redox probe (Fig. 2). In principle, the HET rate can be determined from an individual cyclic voltammogram (CV) by fitting. However, this method is time consuming. We therefore performed a series of numerical cyclic voltammetry simulations as described in electrochemistry text books using in-house Matlab scripts in order to establish a relation between the peak-to-peak separation E_{PP} (Fig. 2a) and k_0 for the ferro/ferricyanide redox probe. Butler-Volmer kinetics with $\alpha = 0.5$, diffusivities of $D_O = 0.76 \times 10^{-5}$ cm^2/s and

Table II. Matsuda number Λ as a function of E_{PP} calculated for the ferro/ferricyanide redox probe.

E_{PP} (mV)	57.7	58.4	59.1	60.7	62.3	64.5	67.7	71.8	77.9	92.3	105.6	121.9
Λ	63.86	31.93	22.35	12.77	8.941	6.386	4.470	3.193	2.235	1.277	0.8941	0.6386
E_{PP} (mV)	143.6	168.3	198.2	251.0	286.8	321.2	357.9	392.8	429.8	487.8	524.7	559.5
Λ	0.4470	0.3193	0.2235	0.1277	0.0894	0.0639	0.0447	0.0319	0.0224	0.0128	0.0089	0.0064

$D_R = 0.63 \times 10^{-5}$ cm²/s for the oxidized and reduced form of the redox probe and a temperature of $T = 298$ K were used. The applied potential protocol for the simulations followed the exact same potential vs. time relations also used for our measurements (starting potential −240 mV vs. equilibrium potential etc.). We have shown previously[9] that this procedure results in an excellent agreement between the simulation results and CVs recorded in the reversible and quasi-reversible regime once experimental parameters such as the concentration of the redox probe and the electrode surface area are matched.

Using a particular scan rate ν as well as k_0 as input parameters, we can extract two numbers from each simulation. The first one is a dimensionless number Λ characterizing the properties of the redox reaction, in a similar form first introduced by Matsuda and Ayabe:[31]

$$\Lambda = \frac{k_0 \left(\frac{D_O}{D_R}\right)^{\alpha/2} RT}{{D_O}^{0.5} F\nu} \quad [1]$$

Here, R and F denote the gas constant and the Faraday constant, respectively. The second number is E_{PP}. This is the difference in potential between the oxidation and the reduction peak. Using the methodology described above for a series of simulations, we determined the relation between E_{PP} and Λ as shown in Figure 2b and reported in Table II. Note that this relation is significantly different from relations shown in text books[31] for $E_{PP} < 70$ mV, as the conditions chosen there (in particular the width of the potential window) differ from the ones used in our simulations and experiments. The calculation results presented in Figure 2b and Table II are specific to the start and switching potentials of the potential program used to control our cyclic voltammetry experiments. Based on the established relation, it is possible to relate any measured value of E_{PP} to the corresponding value of Λ, where value pairs that lie between simulation points are determined by spline interpolation. From the knowledge of Λ, k_0 can be calculated by re-arranging Eq. 1. Values obtained at different scan rates are averaged.

For the two example measurements shown in Figure 2a, this analysis yields the following: In the case of FGS_{60}, we measure a value of $E_{PP} = 64.6$ mV, corresponding to $\Lambda = 6.29$. Using Eq. 1, we obtain an HET rate of $k_0 = 3.3 \times 10^{-2}$ cm/s. In the case of FGS_2, we measure a value of $E_{PP} = 348$ mV, corresponding to $\Lambda = 0.05$ and $k_0 = 2.5 \times 10^{-4}$ cm/s. A comparison of the CV measured with FGS_2 (Fig. 2a) and the calculated CV for $\Lambda = 0.022$ (Fig. 2b, inset) reveals that the experimental and simulated curve shapes are no longer in perfect agreement. The experimental oxidation and reduction peaks are broader than expected in theory, indicating electrode heterogeneities (locally different HET rates) – a behavior that is typically seen in FGS_2 and some highly annealed FGS electrodes. Consequently, for $\Lambda < 0.1$ HET rates must be understood as effective values representing the spatially averaged kinetics of the redox probe.

The estimation of k_0 from EIS measurements proceeds in the following way: Using a classical Randles circuit with constant phase element as an equivalent electrical circuit, we perform a numerical fitting of the data using Matlab (Fig. 2c). From the fit, we obtain the charge transfer resistance R_{CT} which is approximated by the diameter of the (typically depressed) semicircle that appears in the high frequency range as the data is presented in a Nyquist plot. From R_{CT}, we calculate k_0 using the following equation:[31]

$$k_0 = \frac{R \cdot T}{F^2 \cdot R_{CT} \cdot A \cdot C_{eq}} \quad [2]$$

where A is the electrode surface area, and C_{eq} is the ferrocyanide concentration at equilibrium potential (about 240 mV vs. Ag/AgCl).

The EIS measurements shown in Figure 2c correspond to the CVs presented in Figure 2a. For FGS_2, we obtain values of $R_{CT} = 10.2$ kΩ, yielding $k_0 = 2.3 \times 10^{-4}$ cm/s, which is in excellent agreement with the cyclic voltammetry data. With FGS_{60} (Fig. 2c, inset) we obtain $R_{CT} = 29.3$ Ω and $k_0 = 3.25 \times 1\ 0^{-2}$ cm/s which again lies very close to the value determined by cyclic voltammetry.

Results and Discussion

Experiments using the ferro/ferricyanide redox probe.—In Figure 3, we show the rates of HET for FGSs with different degrees of thermal reduction as determined by cyclic voltammetry and EIS in comparison with average rates obtained for glassy carbon and freshly cleaved HOPG (horizontal dashed lines). For FGS_2, k_0 lies in the range from 10^{-4} to 10^{-6} cm/s as determined by cyclic voltammetry. With EIS, significantly lower values were measured occasionally, as indicated by the arrow in Figure 3b. In such cases, the corresponding CVs showed no peaks within the potential window and E_{PP} could thus not be determined. Mildly reduced FGS_4 yields values of k_0 up to 5×10^{-2} cm/s. Upon further reduction, HET rates larger than

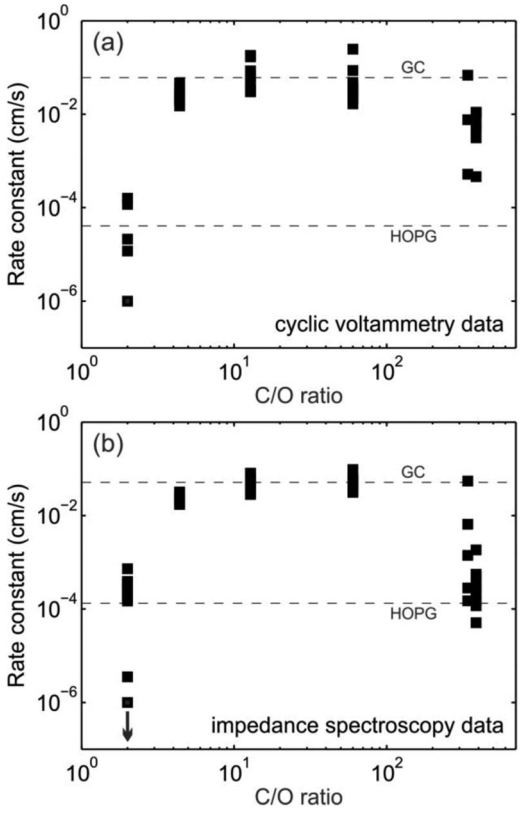

Figure 3. HET rates measured with ferro/ferricyanide on monolayers of thermally reduced graphene oxide as a function of C/O ratio. Results from analysis of (a) CVs and (b) EIS data are shown. Data for FGS_2 that could not be analyzed by cyclic voltammetry due to $E_{PP} > 700$ mV yielding rate constants below 10^{-7} cm/s are represented by the black arrow. Dashed lines indicate average rates of HET obtained for HOPG and glassy carbon (GC).

10^{-1} cm/s are obtained for FGS_{13} and FGS_{60}. Upon thermal annealing, we find that HET rates drop off, reaching values below 10^{-3} cm/s. For each type of FGS, we observed no differences between the data obtained on gold and HOPG substrates.

From our data we infer that the largest HET rates are obtained with those types of FGSs that exhibit intermediate oxygen content and maximum lattice defectiveness as demonstrated in Figure 1a. For FGSs with high oxygen content, such as FGS_2 and FGS_4, we attribute the lower HET rates mostly to an absence of suitable active sites impeding charge transfer. (Redox probes that are not surface site specific such as ruthenium hexamine[32] undergo fairly unimpeded electron transfer on FGS_2 monolayers as electrons can easily tunnel through the FGS_2 monolayer.) Nonetheless, the comparably large electronic resistance of FGS_2[33] might contribute to the observation that electron transfer kinetics of ferro/ferricyanide on FGS_2 are slow. Compared to the data for FGS_4, FGS_{13}, and FGS_{60}, the FGS_2 data show significantly larger scattering – spanning a range of more than two orders of magnitude. This can be explained with a high sensitivity of these measurements to the completeness of the substrate coverage (in case of HOPG substrates) and the effectiveness of the substrate passivation (in case of gold substrates). The relative coverage of monolayers produced by the same approach is reported in our previous work,[14,15] and is typically $90 \pm 5\%$ as determined by SEM. Therefore, uncovered areas in between the sheets are inevitable in our samples. This has a significant effect on the determination of the HET rate in the case of FGS_2. In particular, in the case of HOPG substrates, which can be assumed to exhibit a higher HET rate than the (supposedly completely blocking) FGS_2, the area of HOPG exposed to the electrolyte may lead to an overestimation of the HET rate.

For annealed FGSs, low HET rates might be due to the fact that their structure approaches that of the basal plane of HOPG. This substrate is believed to exhibit poor electron transfer kinetics due to an absence of lattice defects. It is commonly assumed that the presence of defects accelerates electrochemical kinetics, not only for graphene but also for CNTs.[34,35] Recently, the importance of defects for the surface reactivity of FGSs has been demonstrated for catalytic reactions carried out by non-electrochemical routes.[36] However, the low reactivity of the defect-free basal-plane of graphite has recently been challenged by Unwin et al.[37] They studied the electrochemical activity as a function of time and showed evidence that electrochemical reactions on the basal-plane may be slow due to adsorbed contaminants. The large scatter of our data for annealed FGSs could potentially support this view in case of the ferro/ferricyanide redox probe.

From our data it is evident that some HET rates measured with FGS_{13} and FGS_{60} exceed the average HET rate obtained for ferro/ferricyanide on glassy carbon. However, the largest HET rate obtained on one of our glassy carbon electrodes was 1.1×10^{-1} cm/s which lies close to our maximum value obtained with FGS_{60} of $k_0 = 2.5 \times 10^{-1}$ cm/s. We consider this difference to be insignificant and conclude that within our measurement accuracy FGSs do not show any increased electron transfer rates compared to glassy carbon. Furthermore, the HET rates measured on FGSs may be slightly overestimated due to the electrode morphology: We have shown in a recent study of the surface capacitance of FGSs, that our monolayers exhibit a certain degree of roughness, determined by AFM.[15] A detailed analysis of roughness and substrate coverage revealed that the electrolyte-accessible surface area of different FGS monolayers varies by up to 10% and thus may exceed the surface area of a glassy carbon electrode by that amount. This would consequently result in an overestimation of the HET rate on FGS monolayer electrodes of up to 10% for which we do not correct here.

Upon electrochemical reduction, monolayers of FGS_2 can exhibit intermediate rates of HET with respect to the ferro/ferricyanide redox probe (Fig. 4). With increasing negative reduction potential, we observe an increase of the HET rate up to values of $k_0 = 1.4 \times 10^{-2}$ cm/s. Only after excessive electrochemical reduction at potentials of −1.25 V, this trend appears to be reversed. Studies suggest,[38] that electrochemical reduction at potentials around −1 V results in a C/O ratio near 10. At first, one might therefore consider it surprising that HET rates obtained with erFGS electrodes lie one order of magnitude below the largest values obtained, e.g., with FGS_{13}. However, two factors might serve as an explanation for the higher HET rates of thermally reduced FGSs as compared to erFGS: (i) While it can be shown that with increasing reduction temperature and time, the electrical conductivity of thermally reduced FGS increases as the oxygen content is reduced,[39] it is incorrect to assume that the electrical conductivity of FGSs depends on C/O ratio alone, independent of the applied reduction technique. Rather, despite similar C/O ratio, FGS_{13} may in fact be more electrically conducting than erFGS, thus improving electron transfer kinetics through a more rapid diffusion of electronic charge through the electrode material. (ii) Even more importantly, there is indication that erFGS shows significantly lower number density of lattice defects as compared to thermally reduced FGSs.[40] It is therefore plausible that the higher number density of lattice defects in FGS_{13} and FGS_{60} may be the cause of increased HET rates compared to erFGS, as argued above in the comparison of FGS_{13} and FGS_{60} with annealed FGSs and HOPG.

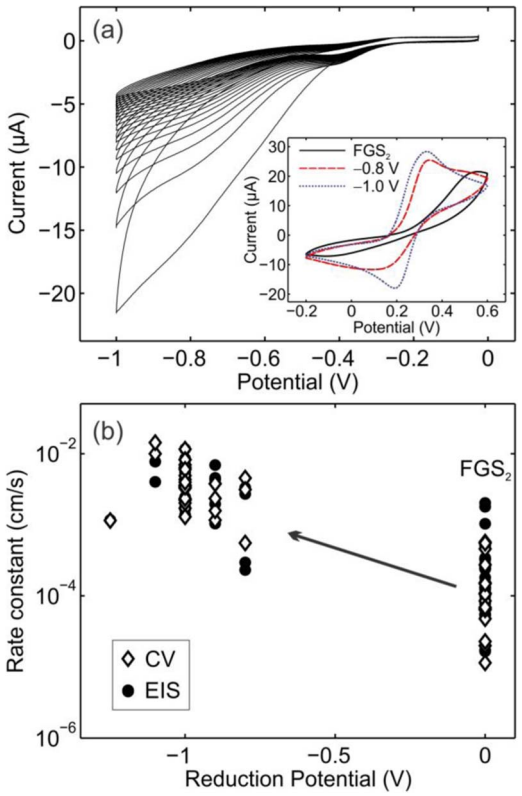

Figure 4. Electrochemical reduction of graphene oxide monolayers. (a) CVs obtained during the electrochemical reduction of graphene oxide on HOPG (20 cycles between OCV and −1 V). The inset shows representative CVs obtained with different types of erFGS. (b) HET rates determined for different types of erFGS as well as graphene oxide monolayers on gold and HOPG.

Pumera et al. studied erFGS in a similar way using drop-cast electrodes and obtained nearly identical results.[38] However, we suspect that the similarity in observed rate constants is due to the superposition of two competing effects: Due to the porosity and roughness of the drop cast films, HET rates were overestimated, and this was likely compensated by an insufficient electronic transport within the electrode film (by itself giving rise to a lower effective HET rate) due to the low C/O ratio in the range of 5 to 10 for those films with significantly increased HET rate compared to FGS_2.

Experiments using biomolecules.—Figure 5 depicts representative CVs obtained with three different types of thermally reduced FGSs as well as glassy carbon and HOPG in the presence of NADH. Here, the measure of electrode performance is the position of the

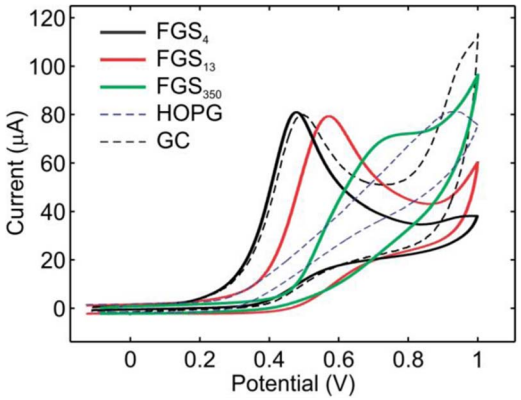

Figure 5. CVs in the presence of NADH for different degrees of thermal reduction in comparison to glassy carbon and HOPG obtained with FGS monolayers on passivated gold substrates.

oxidation peak on the potential axis. The further to the left the peak is located, the lower the overpotential necessary to drive the reaction. While most FGS monolayers require higher overpotentials for NADH oxidation than glassy carbon, mildly reduced FGS_4 shows a slightly reduced overpotential compared to glassy carbon, implying it is more electrocatalytic. This observation is in accordance with recent findings by Pumera et al. who used a combination of electrochemical studies and molecular dynamics calculations to analyze the interactions between NAD^+ molecules in solution and negatively charged functional groups on FGSs.[41] They found particularly large interaction energies between COO^- moieties at the edge of graphene sheets and the positively charged nitrogen atom in the NAD^+ molecule. This view is strongly supported by our FTIR data (Figs. 1b–1c), where it can be seen that absorption bands associated with carboxyl groups and other potentially negatively charged groups such as ketones or phenolic hydroxyls are present to a large extent in FGS_4 reduced at 300°C but almost completely removed at reduction temperatures of 1100°C. Therefore, the low overpotential observed during NADH oxidation on FGS_4 is likely due to favorable specific interactions between the electrode and the redox probe. It is also known, that glassy carbon surfaces are decorated with a variety of oxygen-containing functional groups such as hydroxyl, carbonyl, carboxy, and quinoidal structures.[42] It is therefore expected that glassy carbon yields a result similar to the one obtained with FGS_4. Monolayers of erFGS typically showed NADH oxidation potentials located between those of glassy carbon and FGS_{13}, depending on the specific reduction potential. For a full understanding of the observed differences between the various graphene materials and glassy carbon, it would of course be necessary to study the interaction of NAD^+ with any of the functional groups present on FGSs and glassy carbon individually, which is beyond the scope of this work.

For thermally reduced FGSs, similar trends as with NADH are observed for AA and DA (Figs. 6a–6b). In both cases, the lowest oxidation potentials are seen with the mildly reduced FGS_4. On glassy carbon, AA is oxidized at a significantly larger potential than on both FGS_4 and FGS_{13}. Only erFGS as well as annealed FGS (not shown) yield higher oxidation potentials. Furthermore, with FGS_4 and – to a smaller extent – with FGS_{13}, the oxidation peaks are strongly asymmetrical showing a very rapid rise of the current upon increasing potential. This is indicative of adsorption of the redox probe on the electrode.[31] Such adsorption behavior appears counterintuitive due to the negative charge of the ascorbate anion that should show an unfavorable interaction with many of the negatively charged oxygen species on FGSs. On the other hand, the oxidation of AA is a complicated multi-step process that is known to depend strongly on the presence of surface functional groups as has been studied in detail with glassy carbon electrodes.[43] Based on our experimental observations, we can only conclude that the specific structure and surface chemistry

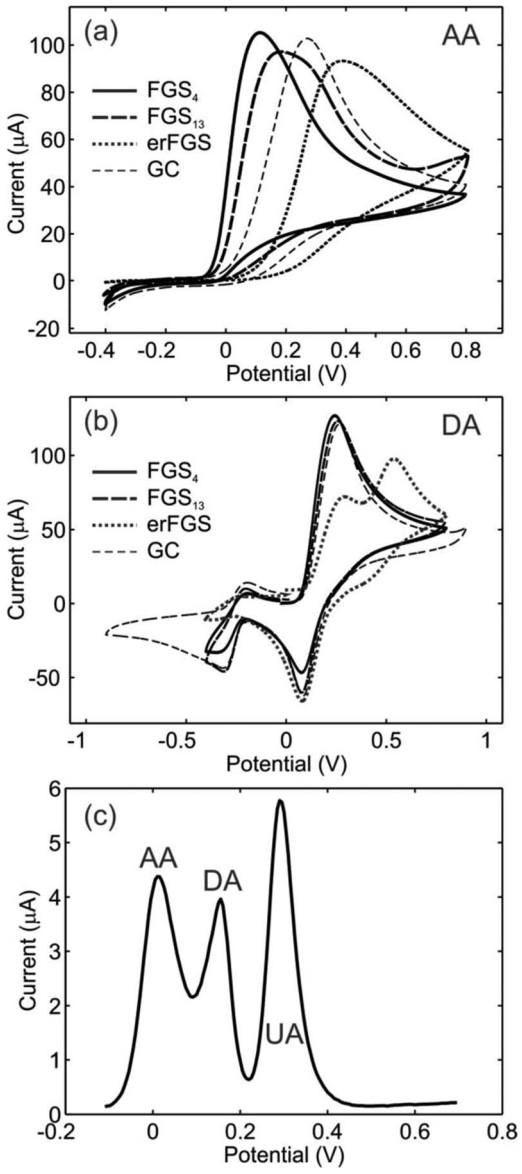

Figure 6. Comparison of the CVs obtained with (a) AA and (b) DA on different types of FGSs on (a) gold and (b) HOPG in comparison to the response obtained with glassy carbon (GC) electrodes. (c) Simultaneous measurement of AA, DA, and UA using a FGS_4 monolayer on HOPG and differential pulse voltammetry.

of FGSs obtained through mild thermal reduction is beneficial for an effective electron transfer as opposed to the type of functional groups (and possibly contaminations) on polished glassy carbon. The performance of glassy carbon electrodes could be improved by surface activation procedures as described in the literature.[44–46]

Dopamine, on the other hand, is protonated at neutral pH and is known to adsorb strongly on all carbon surfaces.[47,48] We consequently find only insignificant differences in the electrochemical responses obtained with thermally reduced FGSs and glassy carbon. Only with erFGS, we obtain a significantly altered response which appears to be a superposition of (spatially separated) high- and low-activity regions. We cannot exclude the possibility that the effective active surface area of erFGS is significantly smaller than the projected surface area of the electrode, and that the second peak is due to the onset of oxidation at inactive sites.

Low-C/O ratio FGS monolayers allow for a highly selective simultaneous detection of AA and DA in the presence of UA as an additional interferrant. Figure 6c depicts a differential pulse voltammetry where

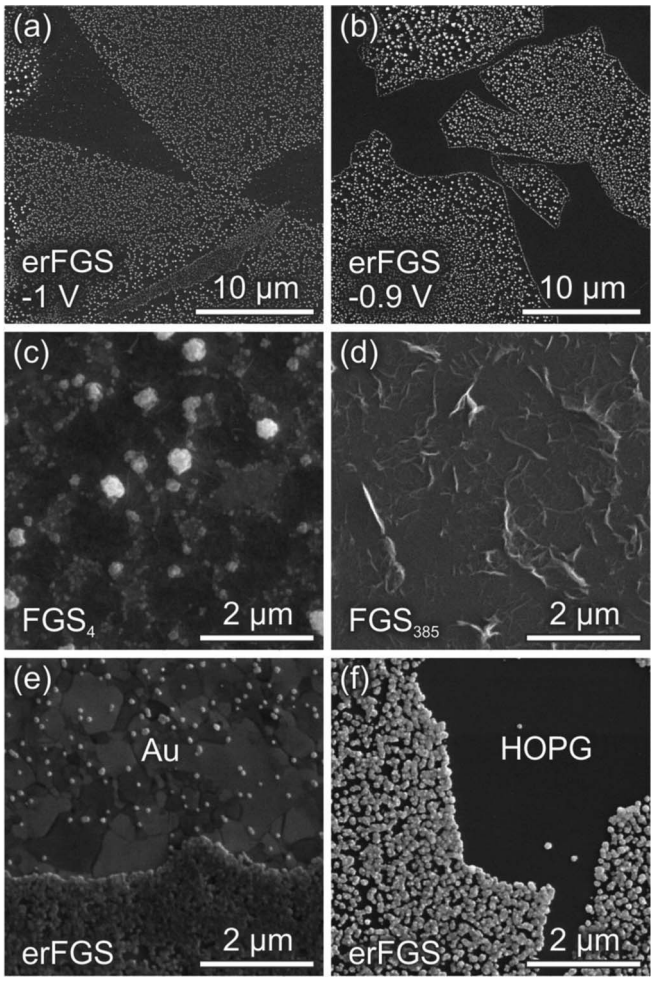

Figure 7. Electrodeposition of copper on electrochemically and thermally reduced graphene oxide. (a–d) Deposition with 2-step method as described in the Experimental section using HOPG (a–b) and gold (c–d) substrates. (e–f) Deposition at fixed potential on erFGS on HOPG reduced at only −0.8 V, giving rise to a larger number of nucleation events. Isolated copper deposits visible on gold in (e) indicated the presence of pin holes in the passivation layer.

we observe three distinct peaks that can be associated with AA, DA, and UA present in the electrolyte.

Electrodeposition experiments.—Electrodeposition of metals can be used as an "indirect" tool to assess the "reactiveness" of an electrode surface by determining the morphology of the metal deposits employing electron or optical microscopy.[49,50] Homogeneous films or densely packed metal deposits can qualitatively indicate a high "reactiveness", while sparse deposition indicates low "reactiveness". However, the latter term does not necessarily describe the intrinsic kinetics of redox reactions but is strongly affected by factors such as electrode wettability (both with respect to the electrolyte as well as the deposited metal) and specific charge (as the metal cations prefer to form metallic nuclei near negatively charged moieties). Furthermore, the chemical environment (e.g., pH) as well as electrolyte concentration and dynamic transport effects in the electrolyte during deposition play important roles.[51] Consequently, electrodeposition results should be regarded to be rather "illustrative" in nature.

In Figure 7, we show selected SEM images of our electrodeposition experiments both with erFGS and thermally reduced and annealed graphene oxide. We find that with erFGS, the sheets are covered with copper particles at an average distance of a few 100 nm. The more mildly reduced erFGS (Fig. 7b) interestingly exhibits a significantly higher copper particle density along the edges of the graphene sheets, suggesting that the −0.9 V reduction procedure left a higher density of negatively charged functional groups at the FGS edges (where copper clusters could be expected to nucleate preferentially) compared to the −1 V case.

With thermally reduced FGS_4, we see a large number of comparably small <100 nm diameter copper particles along the edges of the sheets (which appear darker compared with the background and have diameters of about 1 µm). Additionally, a few larger copper deposits are found occasionally. The plane of the sheets appears to be free of copper deposits. This indicates that after thermal reduction either suitable functional groups are not present on the plane of the sheets, or copper nucleation there would take place at a comparably smaller rate, such that depletion effects due to the presence of early-nucleating deposits at the sheet edges prevent any further nucleation.[51] Annealed FGSs do not exhibit any noticeable copper deposition with the applied −0.65 V potential step. However, in experiments applying −1 V during electrodeposition (not shown), we do observe copper deposits also in the case of annealed FGS, indicating that the observations sensitively depend on the choice of the potential and current program applied. This is also illustrated by Figures 7e–7f. Here, we electroplate copper onto erFGS reduced at −0.8 V using a different electrodeposition protocol, where we simply hold the potential at −0.75 V until a charge of 10 mC has been transferred (in case of a homogeneous deposition of copper, this would yield a copper layer of about 100 nm thickness). This results in a more densely coated FGS monolayer compared to the erFGSs shown in Figures 7a–7b which we attribute to a prolonged nucleation phase that allows also less favorable sites on the electrodes to accumulate copper.

The substrates (i.e., HOPG or thiolated Au) can be considered passive with respect to copper electrodeposition. While on the annealed gold (Fig. 7e), we can see a few deposits which probably nucleated at pin hole defects of the thiol film, the HOPG basal plane shows almost no deposition at all (Fig. 7f). The latter of course depends strongly on the quality of the HOPG used. Lower grade HOPG shows copper deposition along steps which is in agreement with prior studies comparing the electrochemical activity during metal deposition on the edge and basal plane of graphite[52] or on defects of CNTs.[53]

Conclusions

Using a monolayer electrode approach that allows for the assessment of the material-intrinsic electrochemical properties of reduced graphene oxide, we have shown that the rates of electrochemical reactions on these electrodes strongly depend on the type and degree of graphene oxide reduction. For ferro/ferricyanide, FGS electrodes made from highly defective FGS_{13} and FGS_{68} exhibit fast electron transfer kinetics equal to that of a freshly polished glassy carbon electrode. Both with low degrees of reduction and with FGSs annealed at high temperatures, a lack of suitable reactive sites causes low HET rates. Interactions of FGS monolayers with the bio-molecular redox probes NADH, AA, and DA are strongly dependent on the presence of negatively charged, oxygen-containing functional groups, leading – in the case of AA and FGS_4 as well as FGS_{13} – to a substantially enhanced apparent electrocatalytic activity compared to glassy carbon, which might be due to specific adsorption of the AA on the FGS monolayers. The large observed differences in electrochemical kinetics become "visually" evident by comparing the results of electrodeposition experiments on different types of FGSs.

Our work shows that the effectiveness of graphene-based materials in electrochemical applications needs to be assessed with great care and depends highly on the specific electrochemical reaction being studied. Therefore, for different applications such as biosensing, energy conversion, etc., the properties of the graphene material (i.e., structure and number density of defects and functional groups) must be tuned appropriately to yield optimal results. In comparison to the classical electrode material glassy carbon which comprises a functionalized and defective surface structure as well, FGSs may in some cases show superior intrinsic properties. However, based on this

study and our prior work, we conclude that the major advantages of using graphene-based materials in electrochemical applications likely comes from the possibility to manufacture complex, porous electrode architectures (giving rise to the aforementioned beneficial porosity-related effects such as apparent catalytic behavior) and to apply simple and scalable electrode preparation techniques such as screen printing.

Acknowledgments

This work was supported by the Pacific Northwest National Laboratory (operated for the United States Department of Energy by Battelle) under grant Number DE-AC05-76RL01830 and by the Small Business Innovation Research program of the National Science Foundation under grant Number IIP-1142890.

C. P., M. A. P., and I. A. A. declare financial interest in Vorbeck Materials Corp. that manufactures FGSs under the trade name Vor-x.

References

1. M. Pumera, A. Ambrosi, A. Bonanni, E. L. K. Chng, and H. L. Poh, *TRAC - Trend. Anal. Chem.*, **29**, 954 (2010).
2. Y. Shao, J. Wang, H. Wu, J. Liu, I. A. Aksay, and Y. Lin, *Electroanalysis*, **22**, 1027 (2010).
3. D. A. C. Brownson, D. K. Kampouris, and C. E. Banks, *Chem. Soc. Rev.*, **41**, 6944 (2012).
4. A. Ambrosi, C. K. Chua, A. Bonanni, and M. Pumera, *Chem. Rev.*, **114**, 7150 (2014).
5. I. V. Pavlidis, M. Patila, U. T. Bornscheuer, D. Gournis, and H. Stamatis, *Trends Biotechnol.*, **32**, 312 (2014).
6. L. Kavan, J.-H. Yum, and M. Graetzel, *Electrochim. Acta*, **128**, 349 (2014).
7. M. Carbone, L. Gorton, and R. Antiochia, *Electroanalysis*, **27**, 16 (2015).
8. C. Punckt, M. A. Pope, J. Liu, Y. Lin, and I. A. Aksay, *Electroanalysis*, **22**, 2834 (2010).
9. C. Punckt, M. A. Pope, and I. A. Aksay, *J. Phys. Chem. C*, **117**, 16076 (2013).
10. C. Punckt, M. A. Pope, and I. A. Aksay, *J. Phys. Chem. C*, **118**, 22635 (2014).
11. Y. M. Liu, C. Punckt, M. A. Pope, A. Gelperin, and I. A. Aksay, *ACS Appl. Mater. Interfaces*, **5**, 12624 (2013).
12. A. Y. S. Eng, C. K. Chua, and M. Pumera, *Electrochem. Commun.*, **59**, 86 (2015).
13. M.-A. Goulet, M. Eikerling, and E. Kjeang, *Electrochem. Commun.*, **57**, 14 (2015).
14. M. A. Pope, C. Punckt, and I. A. Aksay, *J. Phys. Chem. C*, **115**, 20326 (2011).
15. M. A. Pope and I. A. Aksay, *J. Phys. Chem. C*, **119**, 20369 (2015).
16. A. Dimiev, D. V. Kosynkin, L. B. Alemany, P. Chaguine, and J. M. Tour, *J. Am. Chem. Soc.*, **134**, 2815 (2012).
17. M. A. Pimenta, G. Dresselhaus, M. S. Dresselhaus, L. G. Cancado, A. Jorio, and R. Saito, *Phys. Chem. Chem. Phys.*, **9**, 1276 (2007).
18. K. N. Kudin, B. Ozbas, H. C. Schniepp, R. K. Prud'homme, I. A. Aksay, and R. Car, *Nano Lett.*, **8**, 36 (2008).
19. L. G. Cancado, A. Jorio, E. H. Martins Ferreira, F. Stavale, C. A. Achete, R. B. Capaz, M. V. O. Moutinho, A. Lombardo, T. S. Kulmala, and A. C. Ferrari, *Nano Lett.*, **11**, 3190 (2011).
20. E. Fuente, J. A. Menendez, M. A. Diez, D. Suarez, and M. A. Montes-Moran, *J. Phys. Chem. B*, **107**, 6350 (2003).
21. T. Szabo, O. Berkesi, and I. Dekany, *Carbon*, **43**, 3186 (2005).
22. T. Szabo, O. Berkesi, P. Forgo, K. Josepovits, Y. Sanakis, D. Petridis, and I. Dekany, *Chem. Mater.*, **18**, 2740 (2006).
23. A. Bagri, C. Mattevi, M. Acik, Y. J. Chabal, M. Chhowalla, and V. B. Shenoy, *Nat. Chem.*, **2**, 7 (2010).
24. C.-J. Kim, W. Khan, and S.-Y. Park, *Chem. Phys. Lett.*, **511**, 110 (2011).
25. C. Zhang, D. M. Dabbs, L.-M. Liu, I. A. Aksay, R. Car, and A. Selloni, *J. Phys. Chem. C*, **119**, 18167 (2015).
26. H. C. Schniepp, J. L. Li, M. J. McAllister, H. Sai, M. Herrera-Alonso, D. H. Adamson, R. K. Prud'homme, R. Car, D. A. Saville, and I. A. Aksay, *J. Phys. Chem. B*, **110**, 8535 (2006).
27. M. J. McAllister, J.-L. Li, D. H. Adamson, H. C. Schniepp, A. A. Abdala, J. Liu, M. Herrera-Alonso, D. L. Milius, R. Car, R. K. Prud'homme, and I. A. Aksay, *Chem. Mater.*, **19**, 4396 (2007).
28. D. C. Marcano, D. V. Kosynkin, J. M. Berlin, A. Sinitskii, Z. Sun, A. Slesarev, L. B. Alemany, W. Lu, and J. M. Tour, *ACS Nano*, **4**, 4806 (2010).
29. B. Beverskog and I. Puigdomenech, *J. Electrochem. Soc.*, **144**, 3476 (1997).
30. Y. D. Gamburg and G. Zangari, *Theory and Practice of Metal Electrodeposition*, Springer Science & Business Media, LLC (2011).
31. J. A. Bard and L. R. Faulkner, *Electrochemical Methods*, John Wiley & Sons, New York (2001).
32. R. L. McCreery, *Chem. Rev.*, **108**, 2646 (2008).
33. C. Gomez-Navarro, R. T. Weitz, A. M. Bittner, M. Scolari, A. Mews, M. Burghard, and K. Kern, *Nano Lett.*, **7**, 3499 (2007).
34. C. E. Banks, T. J. Davies, G. G. Wildgoose, and R. G. Compton, *Chem. Commun.*, 829 (2005).
35. C. E. Banks and R. G. Compton, *Analyst*, **130**, 1232 (2005).
36. L.-M. Liu, R. Car, A. Selloni, D. M. Dabbs, I. A. Aksay, and R. A. Yetter, *J. Am. Chem. Soc.*, **134**, 19011 (2012).
37. A. N. Patel, M. G. Collignon, M. A. O'Connell, W. O. Y. Hung, K. McKelvey, J. V. Macpherson, and P. R. Unwin, *J. Am. Chem. Soc.*, **134**, 20117 (2012).
38. A. Ambrosi and M. Pumera, *Chem. Europ. J.*, **19**, 4748 (2013).
39. C. Punckt, F. Muckel, S. Wolff, I. A. Aksay, C. A. Chavarin, G. Bacher, and W. Mertin, *Appl. Phys. Lett.*, **102** (2013).
40. G. K. Ramesha and S. Sampath, *J. Phys. Chem. C*, **113**, 7985 (2009).
41. M. Pumera, R. Scipioni, H. Iwai, T. Ohno, Y. Miyahara, and M. Boero, *Chem. Europ. J.*, **15**, 10851 (2009).
42. B. D. Epstein, E. Dallemol, and J. S. Mattson, *Carbon*, **9**, 609 (1971).
43. I. F. Hu and T. Kuwana, *Anal. Chem.*, **58**, 3235 (1986).
44. M. Poon and R. L. McCreery, *Anal. Chem.*, **58**, 2745 (1986).
45. R. Rice, C. Allred, and R. McCreery, *J. Electroanal. Chem.*, **263**, 163 (1989).
46. P. H. Chen and R. L. McCreery, *Anal. Chem.*, **68**, 3958 (1996).
47. C. D. Allred and R. L. McCreery, *Anal. Chem.*, **64**, 444 (1992).
48. B. D. Bath, D. J. Michael, B. J. Trafton, J. D. Joseph, P. L. Runnels, and R. M. Wightman, *Anal. Chem.*, **72**, 5994 (2000).
49. R. O. Kadara, N. Jenkinson, and C. E. Banks, *Sensor. Actuat. B - Chem.*, **138**, 556 (2009).
50. N. A. Choudhry, R. O. Kadara, N. Jenkinson, and C. E. Banks, *Electrochem. Commun.*, **12**, 406 (2010).
51. D. Grujicic and B. Pesic, *Electrochim. Acta*, **47**, 2901 (2002).
52. C. E. Banks and R. G. Compton, *Analyst*, **131**, 15 (2006).
53. Y. W. Fan, B. R. Goldsmith, and P. G. Collins, *Nat. Mater.*, **4**, 906 (2005).